NUMERICAL CHARACTERIZATION OF CRETAN LUTE SOUND-HOLE ROSETTES

Michail Evangelos Terzakis[1], Cédric Van hoorickx[1], Maarten Hornikx[1], Spyros Brezas[2], Vasilis Dimitriou[2]

[1] *Building Acoustics Group, The Built Environment Department, Eindhoven University of Technology, Eindhoven, The Netherlands*
[2] *Physical Acoustics and Optoacoustics Laboratory, School of Music and Optoacoustic Technologies, Hellenic Mediterranean University, Rethymno, Greece*

This paper is a revised version of the authors' submitted manuscript that was peer-reviewed by at least two anonymous reviewers.

Abstract

Rosettes covering the sound hole are characteristic of traditional Greek long-necked string instruments such as the Cretan lute. Although rosettes are known to influence the resonance of musical instrument cavity, their vibrational and airflow effects remain insufficiently studied. This work numerically examines 27 typical Cretan lute rosette geometries using finite element modal and frequency-response analyses combined with steady-state computational fluid dynamics. All rosettes were modeled with identical material properties and dimensions to isolate geometric effects. FEM eigenfrequencies were verified against physics-based models, presenting a good agreement per mode (MAPE < 5%). Clustering analysis showed that vibrational behavior was primarily governed by perforation rates and ligament patterns which strongly controls airflow. Overall, rosette geometries tend to act as independent tuning factors for soundboard behavior.

Keywords: *lute rosettes, numerical music acoustics, vibrations, airflow*

1. Introduction

The Cretan lute (Figure 1) is a long-necked, fretted string instrument widely used in traditional Greek folk music. It is characterized by a bright timbre and percussive articulation, which render it a central element in both ensemble and solo performance practices. A distinctive structural feature of the instrument is the presence of carved rosettes, covering the sound hole. Although primarily regarded as decorative elements, rosettes may also influence the acoustic performance of musical instruments.

Figure 1: Cretan lute with a rosette assembled.

The role of sound holes in resonance frequencies and radiative behavior has been extensively studied (e.g., [1], [2]). In contrast, the acoustic contribution of rosette designs remains insufficiently explored, particularly for Greek traditional instruments. Perforated rosette geometries significantly influence Helmholtz resonance, soundboard mass, and airflow patterns [3], which in turn influence sound generation.
Prior acoustic studies of Greek instruments focused on soundboards and whole instruments. The vibrational characteristics of ancient Greek tortoise-shell lyres [4], modern pear-shaped bowed lyres [5], and carbon-fiber bouzouki-family soundboards [6], [7] have been examined using experimental and numerical methods. However, the specific role of rosette designs on musical instruments, such as Cretan lute, remain unaddressed. The present study aims to numerically characterize the vibrational modal behavior and responses as well as airflow characteristics of typical Cretan lute rosettes, providing insight into their standalone behavior.

2. Methodology

2.1. Samples

Rosette designs ($N = 27$, Figure 2) were collected from a Greek luthier[1]. The designs represent typical birch plywood rosettes standardized to a diameter of 100 mm and a thickness of 3 mm.

[1] Mazarakis Laser Crafts (`www.mazarakislaser.gr`)

Corresponding author: *m.e.terzakis@tue.nl.*

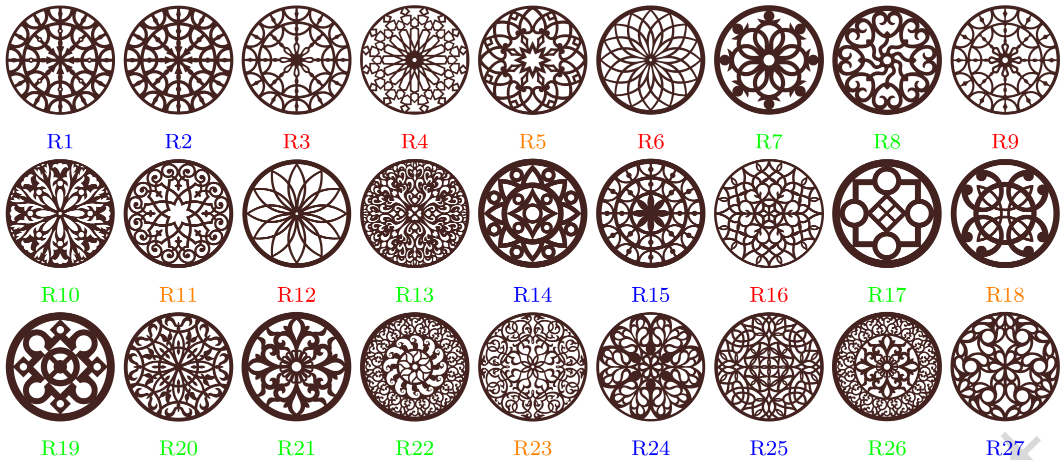

Figure 2: Cretan lute rosette designs. The colouring of the labels indicates the class obtained from the clustering analysis of modal eigenfrequencies presented in Figure 11 (Class 1: blue, Class 2: red, Class 3: orange, Class 4: green).

2.2. Perforation

Rosette designs extracted from PDF images were processed in GIMP to remove the surrounding white background while preserving the internal perforations. The resulting binary masks, representing the material and perforation of rosette designs, were analyzed in MATLAB. An image processing workflow based on grayscale conversion, thresholding, and morphological filtering was applied to segment wood and hole regions. Pixel counts were used to compute perforation ratios, defined as the ratio of hole areas to total rosette area. Segmentation quality was validated through pixel intensity analysis, classification accuracy, and visual overlays of the extracted masks on the original images.

2.3. Vibrational modelling

Following the image processing procedure, 3D rosette geometries were generated. The resulting STL models were imported into COMSOL 6.0, where eigenfrequency analyses were performed using the Finite Element Method (FEM) to identify vibration modes and eigenfrequencies. A fixed boundary condition was applied along the outer perimeter to represent attachment to sound holes. The models were discretized using a tetrahedral mesh, applying orthotropic material properties based on [8] ($\rho = 650$ kg/m^3, $E_x = 11$ GPa, $E_y = 7.0$ GPa, $E_z = 0.8$ GPa, $G_{xy} = 0.8$ GPa, $G_{xz,yz} = 0.16$ GPa, $\mu_{xy} = 0.28$, and $\mu_{xz,yz} = 0.035$).
Vibrational responses were evaluated using a spatially distributed harmonic excitation over the frequency range from 400 Hz to 7k Hz with a resolution of 25 Hz. Seventeen 1 mm radius patches, sixteen in two concentric rings of eight points each, and one at the center, were defined on the top surface to serve as co-located excitation and response locations. In regions with geometric constraints, patches were shifted to the nearest wooden surface. The applied force and the corresponding area-averaged velocity were computed, and complex point mobility was obtained.
As closed-form solutions for the vibration of perforated, orthotropic three-dimensional disks are unavailable, FEM eigenfrequencies are verified using a physics-based scaling procedure identified directly from numerical data. For linear elastic structures, natural frequencies scaled as $f_m \propto \sqrt{K/M}$ [9]. For perforated solids with perforation ratio ϕ_i, the (effective) mass scaled with the remaining solid volume fraction, $M \propto (1-\phi_i)$, while the (effective) stiffness was assumed to follow a power-law dependence, $K \propto (1-\phi_i)^p$, where p is a single global exponent. These yielded the (reduced-order) physics-based model $f_{i,m} = \alpha_m \Theta_i (1 - \phi_i)^p$, where i and m are the design and mode indices, α_m is a mode-dependent coefficient, and Θ_i is a design-dependent topology factor. The global exponent p was identified first by minimizing the total squared error between the FEM and the physics-based eigenfrequencies over all designs and modes, resulting in the optimized value p_{opt}. Then, α_m was computed independently for each mode via least-squares regression across all designs. Finally, Θ_i was obtained for each design as the average, over all modes, of the ratio between the FEM and the corresponding physics-based eigenfrequencies.

2.4. Airflow modelling

Airflow simulations were conducted in COMSOL 6.0 to evaluate the static airflow resistivity of the designs, applying a multi-scale tetrahedral mesh with refined resolution near the rosette surfaces. Each rosette was placed centrally within a bounded cylindrical fluid domain, and a uniform inflow velocity of 0.01 m/s was prescribed at the inlet, yielding a perforation-scale Reynolds number below the inertial threshold and ensuring Darcy-regime flow, with a pressure outlet at the downstream boundary. No-slip conditions were applied to all solid surfaces. The airflow was modeled using a steady-state incompressible laminar formulation. Pressure values were extracted upstream and downstream of rosettes to compute the pressure drop, while the superficial velocity was obtained from the volumetric flow rate. The static airflow resistivity was then calculated according to ISO 9053-1 [10].

2.5. Clustering analysis

Eigenfrequency data were analyzed to assess the influence of perforation and to identify coherent classes of rosette designs. All variables were standardized using z-score normalization to ensure comparability. Clustering was then performed using the k-means algorithm in the combined feature space of perforation percentage and eigenfrequencies. The four-cluster configuration ($k = 4$), was repeated fifty times to ensure robustness, best balances statistical separation and physical interpretability. Cluster regions were visualized using convex hulls, while cluster mean values and standard deviations were used to highlight central tendencies and variability.

3. Results and Discussion

3.1. Perforation

The perforation percentage of each rosette design in Figure 2 was determined using the approach in Section 2.2. An example of this procedure, based on the design R1, is presented in Figure 3. As it is shown, the reconstructed rosette design R1 closely matches the original geometry. The total ornament area comprised 1,099,583 pixels, of which 632,558 pixels corresponded to wood and 467,025 pixels to perforation. The diagnostics further confirmed that wood and hole pixels were classified within the expected intensity ranges, achieving an excellent accuracy. Similar results were obtained across all rosette designs.

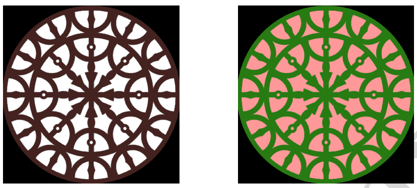

Figure 3: Original (left) and reconstructed (right) R1.

Therefore, the perforation percentage (ϕ) was calculated for each design, and the results are summarized in Table 1, while the cumulative distribution function of the perforation percentages with respect to the normal distribution is presented in Figure 4.

Table 1: Perforation percentage per rosette design.

R_i	ϕ (%)	R_i	ϕ (%)	R_i	ϕ (%)
R1	42.47	R10	36.65	R19	32.09
R2	41.73	R11	42.11	R20	36.96
R3	51.13	R12	54.97	R21	34.85
R4	51.45	R13	30.15	R22	35.77
R5	43.85	R14	28.03	R23	43.63
R6	49.83	R15	37.50	R24	35.16
R7	39.35	R16	47.94	R25	35.85
R8	40.32	R17	41.84	R26	32.32
R9	53.29	R18	38.32	R27	39.51

As can be seen, the perforation percentages of the rosette designs range from 28% in design R14 (lowest perforation) to 55% in design R12 (highest perforation). The perforation percentages ($\mu = 40.63\%$,

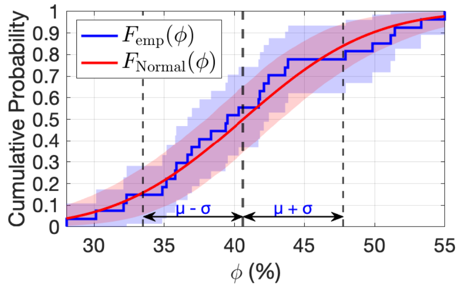

Figure 4: Probability distribution of rosettes' perforation.

$\sigma = 7.14\%$) are consistent with normal distribution, as empirical distribution and Q–Q plot fall within the confidence bounds and Lilliefors test does not indicate a significant deviation from normality. Overall, a perforation variation of nearly one third of the total area is expected to influence the airflow resistivity and, consequently, the acoustic characteristics of the instrument, particularly at higher frequencies.

3.2. Vibrational modes and eigenfrequencies

After generating the 3D rosette geometries, their vibrational characteristics were analyzed using finite element modelling (FEM). Regarding design R1, the corresponding meshed geometry is shown in Figure 5.

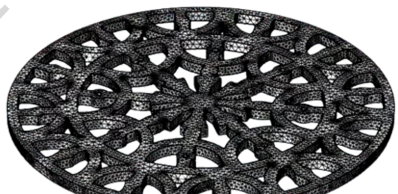

Figure 5: Meshing of R1 design.

The mesh density for each design was selected based on a mesh convergence study, and the results are presented in Figure 6. Designs with thinner structures or ligaments (e.g., R13) required more mesh elements than designs with thicker characteristics (e.g., R18).

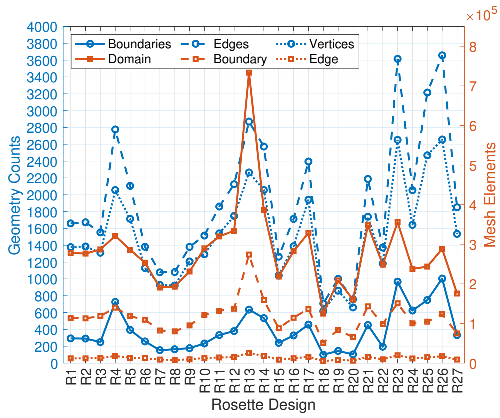

Figure 6: Modelling summaries per rosette design.

The vibrational behavior of rosettes was characterized by their first four eigenmodes (M1–M4), with their eigenfrequencies summarized in Table 2. As both M2 and M3 exhibit split degenerate mode pairs caused by minor geometric and meshing asymmetries, the average frequency of each pair is used as representative value. The fundamental mode (M1) exhibits a global deformation dominated by radial and circumferential displacements, whereas higher-order modes (M2–M4) display increasingly localized deformation patterns. An example of four designs is presented in Figure 7. Rosettes with denser wooden frameworks tend to exhibit higher eigenfrequencies, while designs with larger perforation ratios are more compliant and vibrate at lower frequencies. However, stiffness distribution associated to topology factors, such as ligament connectivity, can significantly affect this relationship. Overall, the eigenfrequency results indicate that rosette vibrational behavior is governed by the balance between perforation ratio and structural connectivity.

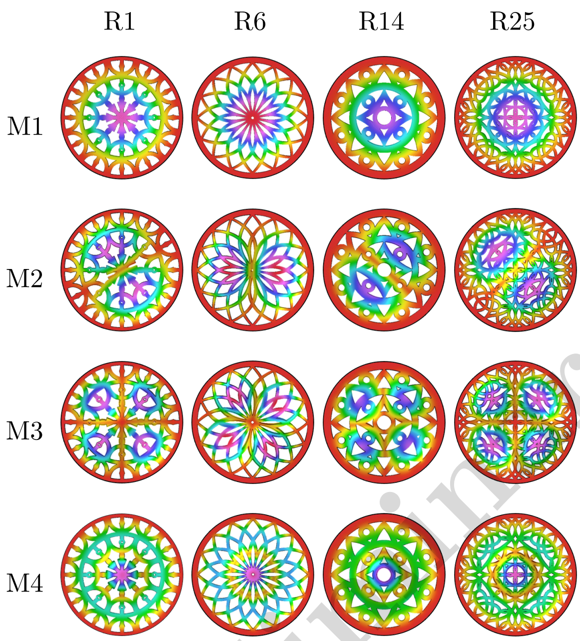

Figure 7: First modes (M1–M4) of four designs.

3.3. Vibrational response modelling

Vibrational responses via mobility were evaluated at seventeen excitation and response locations for all rosette designs. The average mobility for four configurations (R1, R6, R14, and R25) is shown in Figure 8. The first dominant peak corresponds to the fundamental mode, followed by multiple peaks associated with higher-order modes. The configuration with the highest perforation ratio (R6) exhibits a consistent shift of the resonance peaks toward lower frequencies, most notably for the fundamental mode. This indicates a reduction in the (effective) structural stiffness resulting from the increased perforation density. The remaining configurations (R1, R14, and R25) exhibit

Table 2: Eigenfrequencies for M1–M4 per rosette design.

R_i	M1 (Hz)	M2 (Hz)	M3 (Hz)	M4 (Hz)
R1	1131.2	2220.1	3126.5	3602.1
R2	1136.2	2238.7	3146.3	3654.0
R3	1047.3	2061.7	2950.2	3274.5
R4	762.7	1715.7	2788.5	3137.8
R5	804.8	1595.3	2661.0	2944.3
R6	838.6	2006.0	2810.8	3752.2
R7	961.5	1927.4	2788.7	3137.2
R8	803.0	1713.4	2762.7	2971.5
R9	966.5	1980.8	2866.1	3146.1
R10	1096.0	2018.8	2531.4	2900.4
R11	756.0	1519.8	1952.2	2614.9
R12	867.0	2052.2	2910.1	3385.1
R13	941.4	1740.2	2536.5	3210.9
R14	1130.3	2054.4	3286.1	3634.1
R15	1114.0	2193.7	3344.4	3851.0
R16	958.9	1869.8	3001.9	3406.9
R17	930.0	1843.5	2893.5	3412.5
R18	824.0	1497.9	2197.4	2852.8
R19	943.5	1917.3	2990.2	3399.6
R20	938.6	1880.9	2761.2	3532.0
R21	915.4	1936.3	2880.4	3530.8
R22	1023.2	1759.3	2703.0	3323.2
R23	657.0	1244.7	1983.3	2260.0
R24	1117.8	2254.4	3416.4	4192.0
R25	1097.4	2045.0	3173.3	3690.5
R26	1021.1	2009.8	2988.2	3342.5
R27	1043.8	2067.2	2999.8	3601.9

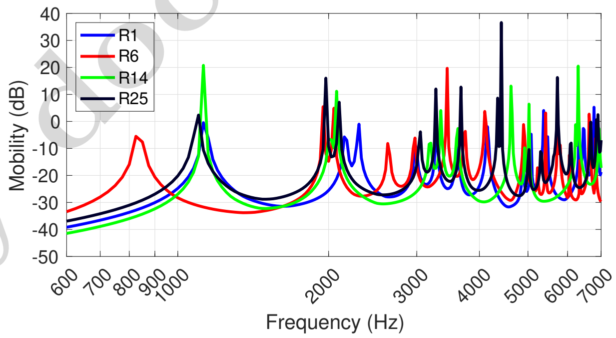

Figure 8: Average mobility for four designs.

closely aligned resonance frequencies and comparable mobility levels, indicating that differences in stiffness distribution may compensate for variations in mass reduction associated with the perforation ratio.

3.4. Vibrational modelling verification

FEM eigenfrequencies were verified against scaled-model eigenfrequencies for the first four modes of each design, and the results are presented in Figure 9. For all modes, the data cluster closely around the identity line, with a Mean Absolute Percentage Error (MAPE) lower than 5%, indicating that the proposed scaling model accurately captures the dominant trends of the numerical results. The remaining scatter is attributed to genuine geometric effects.

Focusing on the topology factor Θ for each design and mode, the results are presented in Figure 10. As can be seen, Θ exhibits relatively small variation across vibration modes for the majority of designs (i.e., 89% of designs present coefficient of variation (CV) values below 10%), indicating weak dependence on vibra-

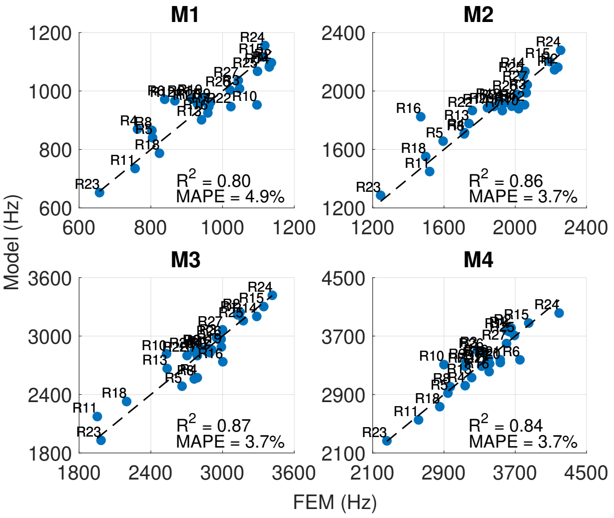

Figure 9: Verification of FEM and physics-based eigenfrequencies per mode. Dashed line denotes perfect agreement.

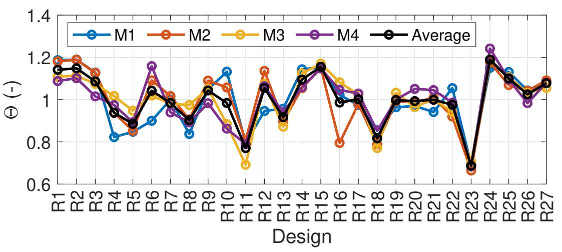

Figure 10: Topology factor Θ per design and mode.

tion mode and thus supporting the use of the mean Θ across modes for each design. The median values across all modes are found to lie around 1.00, while the overall range is bounded between 0.66 and 1.24. This behavior suggests that the perforation pattern primarily modifies the global stiffness of the structure. Designs with lower values of Θ correspond to inefficient load paths and weak ligament connection distribution (e.g., R11 and R23), while higher values indicate stiff ligament connection distribution (e.g., R15, and R24). Consequently, the numerical results are validated not through exact analytical agreement, but through consistency with fundamental mechanical principles governing stiffness, mass, and modal behavior in perforated disks.

3.5. Clustering analysis

The relationship between rosette perforation and modal eigenfrequencies (M1–M4) was examined using a four-cluster classification (Figure 11). For M1, the clusters occupy relatively distinct frequency ranges, although a small degree of overlap between some classes can be observed. For M2–M4, the clusters remain clearly separated across the range of perforation ratios. This behavior suggests that M1 reflects a more global structural response, whereas M2–M4 become increasingly sensitive to local geometric features.

Designs with similar perforation occur in different

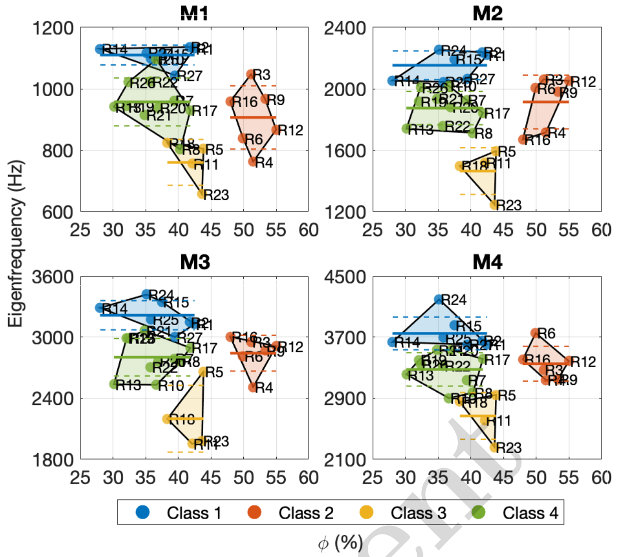

Figure 11: Eigenfrequency clustering as a function of perforation for rosette designs. Solid and dashed lines show class mean and standard deviation.

clusters, indicating that the perforation ratio alone is not sufficient to describe the dynamic behavior of the rosette patterns. Examination of the corresponding geometries suggests that the clusters are associated with different ligament topology characteristics (see Figure 2). Class 1 contains designs with pronounced radial ligament connections linking the centre and the outer boundary, Class 2 contains geometries with relatively thin and densely distributed ligaments, Class 3 contains highly dense patterns with less regularly distributed ligaments, and Class 4 includes designs with comparatively thick ligaments and a more symmetric radial arrangement. These geometric characteristics provide a qualitative interpretation of the clustering observed in the modal frequency results.

3.6. Static airflow resistivity

The static airflow resistivity was evaluated for all rosette geometries based on Section 2.4. The relative velocity magnitude for four designs is presented in Figure 12. The static airflow resistivity values per design was also calculated and the results are summarized in Table 3, exhibiting variability across the designs, ranging from 39.43 Ns/m^4 (R9) to 163.11 Ns/m^4 (R13), corresponding to a more than fourfold difference.

Table 3: Static airflow resistivity (σ) per design.

R_i	σ (Ns/m^4)	R_i	σ (Ns/m^4)	R_i	σ (Ns/m^4)
R1	59.35	R10	85.65	R19	103.86
R2	60.19	R11	64.95	R20	89.55
R3	43.52	R12	48.75	R21	87.89
R4	52.86	R13	163.11	R22	113.16
R5	60.62	R14	114.86	R23	82.16
R6	46.86	R15	81.33	R24	102.63
R7	76.85	R16	50.45	R25	95.11
R8	68.24	R17	74.37	R26	120.54
R9	39.43	R18	78.91	R27	70.19

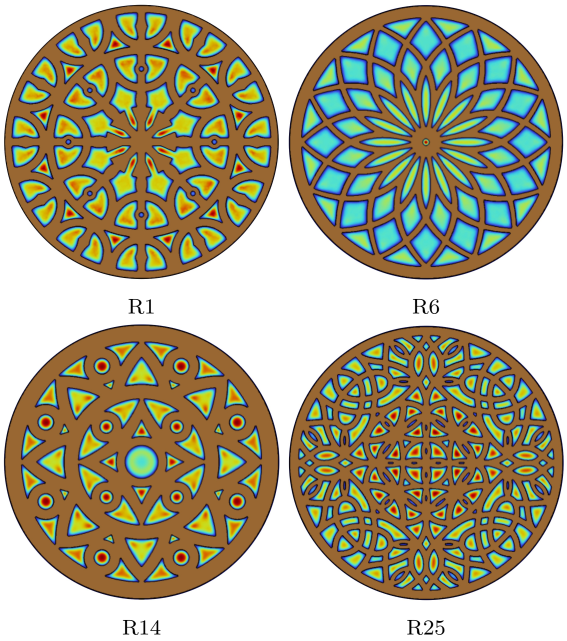

Figure 12: Relative velocity magnitude for four designs through the perforations (red: high, blue: low).

Finally, a power-law relationship between perforation percentage and static airflow resistivity was obtained in Figure 13. The low residual dispersion (0.15 in log space, 16% relative error), the inclusion of 92.6% of the data within the ± 2 standard deviations of the residuals, and the limited leave-one-out variation associated with the designs exceeding the $4/N$ Cook's distance threshold (R12-R14; $\max\{|\Delta n|\} = 0.13$), confirm a robust scaling dominated by perforation.

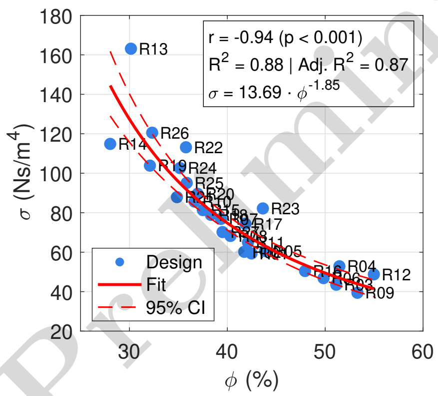

Figure 13: Static airflow resistivity versus perforation.

4. Conclusion

This study presents a systematic numerical investigation of the vibrational behavior of Cretan lute soundhole rosettes under controlled conditions, with material properties, diameter, and thickness held constant. By isolating geometric effects, the influence of rosette perforation on vibrational response and airflow resistivity was quantified, demonstrating that rosette design can act as an independent "tuning" parameter. The results establish a baseline understanding of how rosette geometry affects modal behavior and airflow characteristics, providing a first step toward a more comprehensive assessment of rosette functionality.
Future work will extend this investigation to coupled analyses involving rosettes integrated into soundboards and complete instruments. Experimental measurements and advanced numerical simulations will be employed to evaluate rosette–soundboard interactions and their impact on sound radiation. These efforts aim to bridge the gap between isolated rosette behavior and whole-instrument acoustics, contributing to a more complete understanding of the acoustic role of rosette designs in traditional string instruments.

References

[1] N. H. Fletcher and T. D. Rossing, *The Physics of Musical Instruments*. New York, NY: Springer New York, 1998.

[2] S. D. Bellows and D. Nakayama, "An investigation of the f-hole shape's influence on the modal response of the violin," *Acta Acustica*, vol. 8, p. 67, 2024.

[3] H. T. Nia, A. D. Jain, Y. Liu, M.-R. Alam, R. Barnas, and N. C. Makris, "The evolution of air resonance power efficiency in the violin and its ancestors," *Proceedings of the Royal Society A: Mathematical, Physical and Engineering Sciences*, vol. 471, no. 2175, p. 20 140 905, 2015.

[4] E. Bakarezos et al., "Vibrational analysis of the top plates of traditional Greek string musical instruments," in *13th International Congress on Sound and Vibration*, Vienna, Austria, 2006.

[5] E. Bakarezos, V. Vathis, S. Brezas, Y. Orphanos, and N. A. Papadogiannis, "Acoustics of the Chelys - An ancient Greek tortoise-shell lyre," *Applied Acoustics*, vol. 73, no. 5, pp. 478–483, 2012.

[6] S. Brezas et al., "An Integrated Method for the Vibroacoustic Evaluation of a Carbon Fiber Bouzouki," *Applied Sciences*, vol. 13, no. 7, p. 4585, 2023.

[7] S. Brezas et al., "Vibration analysis of 3D printed cymbals and Tzouras top plates," *INTER-NOISE and NOISE-CON Congress and Conference Proceedings*, vol. 270, no. 5, pp. 6741–6749, 2024.

[8] F. P. Mechel, Ed., *Formulas of Acoustics*. Berlin, Heidelberg: Springer, 2008.

[9] L. Cremer, M. Heckl, and E. E. Ungar, *Structure-Borne Sound: Structural Vibrations and Sound Radiation at Audio Frequencies*, 3rd ed. Springer, 2005.

[10] ISO, "ISO 9053-1: Acoustics: materials for acoustical applications, determination of airflow resistance, Part 1: static airflow method," *International Organization for Standardization*, 2018.